Electrospun TiO_2/SnO_2 Nanofibers with Innovative Structure and Chemical Properties for Highly Efficient Photocatalytic H_2 Generation

Siew Siang Lee, Hongwei Bai, Zhaoyang Liu, and Darren Delai Sun**

School of Civil & Environmental Engineering, Nanyang Technological University, Singapore 639798

Tel: +65-6790-6273; Fax: +65-6790-0676

To whom should be addressed: zyliu@ntu.edu.sg; ddsun@ntu.edu.sg

RECEIVED DATE (to be automatically inserted after your manuscript is accepted if required according to the journal that you are submitting your paper to)

Abstract. Innovative TiO_2/SnO_2 nanofibers were fabricated via electrospinning an innovated precursor solution and used for photocatalytic H_2 generation. The nanofibers exhibited greatly enhanced H_2 evolution rate compared to bare TiO_2 nanofiber and P25. The enhanced efficiency of the TiO_2/SnO_2 nanofibers was attributed to its excellent synergistic properties: 1) its good mesoporosity; 2) the red-shift of absorbance spectra to enhance light absorbance capability; 3) its long nanofibrous structure and 4) anatase TiO_2 - rutile TiO_2 - rutile SnO_2 ternary junctions favorable for the separation of electrons and holes. Based on our experimental results, the optimum ratio of TiO_2/SnO_2 nanofibers with 3% Sn demonstrated the highest efficiency in H_2 generation.

Keywords: Electrospinning, Hydrogen generation, Nanofibers, SnO_2, TiO_2

1. Introduction

Hydrogen (H_2) as an ideal clean energy source has attracted large attention by researchers [1] in response to the pressing global warming issue particularly from the utilization of fossil fuel. Photocatalytic H_2 generation from water splitting is one of the promising long-term solutions to tackle the issue [2-4]. TiO_2-based semiconductor has been widely-studied for H_2 production since it was first reported by Fujishima and Honda in 1972 [5-9]. However, it has inherent rapid recombination of photo-generated electron-hole pairs and wide band gap [10] resulting in low photocatalytic activity for the production of H_2 from water which restricts its practical applications.

Coupling TiO_2 with another semiconductor such as SnO_2 could modify and improve its photocatalytic activities [2, 11]. A few studies have reported that addition of SnO_2 into TiO_2 nanoparticles could promote UV-vis light absorption [12, 13], as well as inducing the formation of anatase TiO_2 - rutile TiO_2 heterojunctions thus enhancing charge separation [2]. However, photocatalytical nanoparticles tend to form aggregates which serve as recombination centers for the photogenerated electrons and holes [14]. On the other hand, TiO_2 nanofibers demonstrated higher photocatalytic activity than TiO_2 nanoparticles owing to its intrinsic properties such as: (1) one-dimensional long structure promoting charge transfer [15]; (2) high porosity and large surface area enhancing mass transfer and light utilization rate; and (3) lower tendency to form aggregates that impedes the recombination of photogenerated electrons and holes [14].

Electrospinning is a versatile method to tune and control the morphology and chemical composition of nanofibers [16]. Recently, our group has reported a novel fully-exposed side-by-side bicomponent TiO_2/SnO_2 nanofibers obtained from electrospinning. This bicomponent TiO_2/SnO_2 nanofibers exhibited excellent photocatalytic activity as a result of its nanofibrous morphology and special heterojunction structure which retard the recombination of photogenerated electrons and holes [17]. However, the benefit from the heterojunction was limited only to the central joint where both TiO_2 and SnO_2 components were in contact on this nanofiber. Thereafter, Hwang et al [18] reported the synthesis

of SnO_2-embedded TiO_2 nanofibers with enhanced contact area between TiO_2 and SnO_2 for organic photo-oxidation. However, there was no improvement on its porosity, surface area, and light utilization rate which also dictate the photocatalytic reaction. Therefore, researchers are still searching for ways to fabricate TiO_2/SnO_2 encompassing benefits of long nanofibrous morphology, modified electronic properties, high dispersion of heterojunctions, and enhanced porosity, surface area, and light absorption.

To date, there has not been any report on H_2 generation potential over TiO_2/SnO_2 nanofibers [19-21]. Herein, for the first time, TiO_2/SnO_2 nanofibers combining the advantages of SnO_2 coupling and their nanofibrous structure was successfully synthesized via electrospinning of an innovative precursor and used for H_2 generation. Briefly, SnO_2 could be easily incorporated into TiO_2 at any amount by improvising the preparation of precursor solution from our previous work [17]. Instead of separate preparation, precursor solutions for TiO_2 and varying SnO_2 were mixed together using a magnetic stirrer without high temperature, high speed mixing, dispersive equipment, or corrosive chemicals [18, 22]. The as-synthesized TiO_2/SnO_2 nanofibers exhibited remarkably enhanced H_2 generation rate than bare TiO_2 nanofibers and the benchmark P25 photocatalyst. The nanofibers were well-characterized and the optimum Sn content and factors affecting its H_2 evolution efficiency were determined and discussed, as follows.

2. Experimental

2.1 Preparation of bare TiO_2 and TiO_2/SnO_2 nanofibers

Ethanol and acetic acid were mixed at a ratio of 4:1 by volume. The polyvinylpyrolidone (PVP; M_W=1 300 000) (7 wt%) was then dissolved in the mixture, followed by the addition of appropriate amount of $Ti(oBu)_4$ and $Sn[CH_3(CH_2)_3CH(C_2H_5)CO_2]_2$ to prepare a blend consisting of 1% mol Sn (1% Sn), 3% mol Sn (3% Sn), 6% mol Sn (6% Sn), 10% mol Sn (10% Sn) and 40% mol Sn (40% Sn), respectively. Instead of separate preparation, precursor solutions for TiO_2 and varying SnO_2 were mixed together at

room temperature using a magnetic stirrer for 6 hours to obtain a homogenous clear solution. The morphology was controlled by maintaining the humidity at < 40% using N_2 gas throughout the electrospinning process to prevent pre-mature hydrolysis of the precursor solution [16, 23]. The same procedure was employed to prepare the precursor for bare TiO_2 nanofiber (0-ST) but without addition of SnO_2 precursor. The respective precursor solution was loaded into a hypodermic syringe with a 1.1 mm diameter stainless steel nozzle [23]. An electrical potential of 19 kV was applied between the nozzle and an aluminium foil collector. A dense nanofiber webs were consequently obtained at the collector. The electrospun nanofibers were left in air for at least 2 hours to enable complete hydrolysis. Then, the hydrolysed electrospun nanofibers were calcined in the air at 450ºC for 30 minutes to obtain TiO_2/SnO_2 nanofibers.

2.2 Characterization

The morphology of the electrospun nanofibers was studied using a field-emission scanning electron microscope (FESEM, JEOL JSM-6340F and HITACHI SU 70) as well as the transmission electron microscope (TEM, JEOL JSM-1400 at 200 kV). The crystallization and crystal lattice of the composite nanofibers were observed on the high resolution transmission electron microscopy (HRTEM, JEOL JEM-2010) working at an accelerated voltage of 200 kV. The crystalline structure was obtained using a Bruker D8 Advance X-ray diffractometer (XRD) with monochromated high-intensity Cu Kα radiation (λ = 1.5418 Å). Scherrer equation which is well-used to measure the crystal size according to the XRD pattern was adopted for the estimation of nanocrystalline size. The Scherrer Equation is $L = K\lambda / \beta \cos \theta$ where L, K, λ, β, and θ are size of particles in nm, a constant of 0.891, wavelength of X-ray, full width at half maximum (FWHM) of the XRD peak, and angle of diffraction, respectively [10, 24]. The content of anatase TiO_2 relative to rutile TiO_2 phase was quantified based on the equation $X_A = 1/(1 + 1.26I_R/I_A)$, where X_A denotes content of anatase phase, and I_R and I_A are intensities of the most intense XRD peaks for anatase and rutile phases, respectively [24]. X-ray photoelectron spectroscopy (XPS) was carried out using a Kratos Axis Ultra Spectrometer with a monochromic Al Kα excitation source at

1486.7 eV, with a voltage of 15 kV and an emission current of 10 mA. All binding energies were referenced to C 1s at 284.6 eV. Elemental composition of the photocatalyst was analyzed using an energy dispersive X-ray spectrometer (EDS) attached to the TEM (JEOL JSM-1400). The Brunauer, Emmett, and Teller (BET) specific surface area were determined at liquid nitrogen temperature (77 K) using a Micromeritics ASAP 2040 system. The samples were degassed at 200ºC for 3 hours prior to measurement. The Barret-Joyner-Halenda **(**BJH) method was employed to obtain the pore size distribution of the photocatalysts. The Thermo Scientific Evolution 300 UV-Vis spectrometer (Thermo Fisher Scientific, Massachusetts, USA) equipped with the integrating sphere and a xenon lamp source was used to record the absorption spectra of the photocatalysts. The spectra were further analyzed to obtain new indirect bandgap energy of the photocatalysts by the Kubelka-Munk function which converts diffusive reflectance measurements into the equivalent absorption coefficients [24, 25]. It is the photon energy (hv) value when $[F(R_\infty)]^{0.5}=0$, obtainable when the vertical segment of the plot of $[F(R_\infty)]^{0.5}$ against hv is extended to intersect the X-axis (hv) [26].

2.3 Photocatalytic H_2 generation

After calcination at 450ºC for 30 minutes, the as-prepared TiO_2/SnO_2 nanofibers were used for photocatalytic H_2 evolution in a methanol/water mixture. Schematic 1 illustrates the schematic diagram of the suspended system of H_2 generation reactor setup. The photocatalytic H_2 generation test was carried out in an inner irradiation type Pyrex reactor with a volume of 270 mL with a 400W high pressure Hg lamp (Riko, UVL-400HA) as the light source. This lamp emits light source within the UV-visible range from 250 – 600 nm, with peak irradiation at 365 nm, 430 nm, 540 nm, and 580 nm. The distance between the light source and the suspended photocatalysts was approximately 1.0 cm. Re-circulated tap water was utilized as heat exchange cooling water to maintain a constant reactor temperature of 298K (25ºC). The TiO_2/SnO_2 nanofibers were suspended at a concentration of 0.5 g/L into sacrificial reagent comprising 1:9 v/v methanol-water mixtures. Prior to irradiation and reaction, the reactor was purged with nitrogen gas for 30 minutes to de-aerate the reactor. Subsequently, the

slurry mixture was continuously mixed using a magnetic stirrer to ensure homogeneity throughout the reaction. Gas produced from the photocatalytic reaction was analyzed using a TCD-type gas chromatography (Agilent 7890A, HP-PLOT MoleSieve/5A) [27, 28]. The as-prepared bare TiO_2 nanofibers and P25 were also tested for H_2 generation for comparison.

3. Results and discussion

Figs. 1(a)-(b) show the morphology of the electrospun nanofibers measured by FESEM. The length of the nanofibers was more than 10 um after calcination. The diameter was less than 100 nm and was highly uniform along the entire length without any beads. The aspect ratio was around 30-50, which was a typical nanofibers structure. Fig. 1(b) clearly illustrates the nanofibrous structure of the nanofibers. The surface was rough and porous due to the burning of PVP during calcinations.

The TEM image in Fig. 2(a) shows the microstructure of the nanofiber with a diameter of approximately 100 nm. The corresponding selected area electron diffraction (SAED) pattern in the insert of Fig. 2(a) suggests that the TiO_2/SnO_2 nanofibers were polycrystalline [22, 29]. In the EDS spectrum observed from Fig. 2(b), peaks of Ti and Sn were prominent. The mapping of a single nanofiber as shown in Figs. 2(c)-(e) depict that all the main elements (Ti, Sn, and O) were well-dispersed throughout the bulk of the nanomaterial.

To further elucidate on the crystal structures of the TiO_2/SnO_2 nanofibers, HRTEM analysis was carried out for the composite nanofibers with 6% mol Sn. The bright field TEM images at different magnifications in Fig. 3(a)-(b) showed clear mass contrast between Ti (light spot) and Sn (dark spot) owing to their different atomic weights [30, 31]. The images also revealed good dispersion of Sn in the TiO_2/SnO_2 nanofibers. The high magnification HRTEM image in Fig. 3(c) obviously indicated three distinctive lattice fringes of 0.325 nm, 0.296 nm, and 0.335 nm; which could be ascribed to the (101) plane of anatase TiO_2, the (110) plane of rutile TiO_2, and the (110)

plane of rutile SnO_2, respectively [18, 26, 32]. Fig. 3(c) also indicated the overlapping of mixed fringe lattices, suggesting the presence of mixed phases of well-crystallized anatase TiO_2/rutile TiO_2/rutile SnO_2 heterojunctions within the composite nanofibers [26]. In addition, the lattice fringes of rutile SnO_2 appeared consistently on the dark part of the nanofibers, which served as another good indication that it could be attributed to rutile SnO_2. Meanwhile, anatase TiO_2 and rutile TiO_2 were observed on the light part of the nanofibers.

The crystal structures of TiO_2/SnO_2 nanofibers were further examined using XRD. As shown in Fig 4(a), the TiO_2/SnO_2 nanofibers were indexed to anatase TiO_2 phase (JCPDS file No. 21-1272) at Sn content below 3% while SnO_2 peak was not discernable at all due to the detection limit of the XRD [33]. At a composition of 3% Sn and beyond, peaks corresponding to rutile TiO_2 phase (JCPDS file No. 21-1276) as well as rutile SnO_2 phase (JCPDS file No. 41-1445) started to appear in addition to the anatase TiO_2 phase, but with considerably low rutile SnO_2 peaks. The weak peak of rutile SnO_2 phase was ascribed to the high dispersion of the Sn species within the bulk of the photocatalysts therefore rendering none or too little SnO_2 on the surface for detection by the XRD [27, 33]. A close-up XRD pattern of the TiO_2/SnO_2 nanofibers with 3% mol and 6% mol Sn across the region of $2\theta = 26^\circ - 40^\circ$ has been plotted against that of the pristine TiO_2 nanofibers to enable a clearer visualization on the phase existence within the composite nanofibers (Fig 4(b)). The sharp peaks at 2θ of 25.10°, 26.50°, and 27.50° in composite nanofibers with 6% mol Sn could be ascribed to the (101) peak of anatase TiO_2, the (110) peak of rutile SnO_2, and the (110) peak of rutile TiO_2, respectively [20, 22, 34, 35]. This observation is in good agreement with the HRTEM image in Fig.3(c); where the (101) plane of the anatase TiO_2, the (110) plane of rutile TiO_2, and the (110) plane of rutile SnO_2 were centered at d-spacing of 0.325 nm, 0.296 nm, and 0.335 nm, respectively. A similar XRD pattern in which the anatase TiO_2, rutile TiO_2, and rutile SnO_2 phases co-existed was also reported by Zhang et al. (2009) for their TiO_2/SnO_2 nanofibers [22]. Zhang et al. (2009) also observed the strengthening peak for rutile TiO_2 at higher Sn loading of 10% mol and above [22]. In another study, Hirano et al. (2011) has reported the co-existence of anatase TiO_2 and rutile TiO_2 at Sn loading of 10 – 20% mol in the composite nanoparticles synthesized via hydrothermal method [31]. However, at Sn loading of 30% mol and above, they observed XRD pattern shifting from rutile TiO_2 into rutile SnO_2 [31]. Possible explanation to this discrepancy could be the different synthesis methods, thus producing different materials of unique crystal structure. On the basis of the

close-up XRD pattern (Fig. 4(b)) and the HRTEM image (Fig. 3(a)-(c)), it is reasonable that the anatase TiO_2/rutile TiO_2/rutile SnO_2 heterojunctions were present in the TiO_2/SnO_2 nanofibers. Table 1 summarizes the calculated percentage and crystalline size of anatase TiO_2 phase decrease with increasing Sn content. There was broadening of the most intense anatase TiO_2 peak at 2θ value of 25.1° which corresponded well to smaller crystalline size based on the Scherrer equation [24]. Decrease in the crystalline size suggests that there was anatase TiO_2 crystal lattice defect following the incorporation of Sn which promoted the formation of rutile TiO_2 at a lower transitional temperature [10, 24]. This justifies the diminishing peak of anatase TiO_2 phase with increasing Sn content in the XRD patterns. The presence of the ternary phases is expected to facilitate photogenerated electrons and holes separation thus increasing their availability for a more efficient photocatalytic activity.

The chemical composition of the TiO_2/SnO_2 nanofibers was studied by XPS analysis. The results were observed in Fig. 5(a) – (d). The binding energy for C1s peak at 284.6 eV was used as the reference for calibration. The survey spectrum as presented in Fig. 4(a) confirms that only Ti, Sn, and O were present in the composite TiO_2/SnO_2 nanofibers, which are in consistent with the EDS spectrum. High resolution XPS spectrum of Ti 2p, Sn 3d, and O 1s were observed in Fig. 5(b) – (d), respectively. The peaks in the Ti 2p spectra (Fig. 5(b)) were indicative of Ti $2p_{3/2}$ and Ti $2p_{1/2}$ of Ti^{4+} [17, 27], located at the binding energy of 457.8 eV and 464.0 eV, respectively. As shown in Fig. 5(c), the symmetrical peaks located at binding energy of 486.0 eV and 494.0 eV were ascribed to the Sn $3d_{5/2}$ and Sn $3d_{3/2}$ of Sn^{4+} [17, 36], respectively. Fig. 5(d) shows the asymmetrical peak of O 1s spectrum consisting of three smaller peaks. The peak at binding energy of 528.9 eV was attributed to the O in TiO_2 and SnO_2 [27, 37], whereas the peaks at higher binding energy of 531.2 eV and 533.0 eV were indicative of surface contamination by hydroxyl and carbonate groups respectively, from the atmosphere [27, 37].

The surface structures of the prepared TiO_2/SnO_2 nanofibers were analyzed by N_2 sorption-desorption isotherm technique. The curve (Fig. 6(a)) revealed type IV isotherm with obvious H3-type hysteresis

behaviour according to IUPAC classification, which characterized the nanofibers to be mainly mesoporous [38]. The BET specific surface area of the composite nanofibers was promoted by Sn coupling and is shown in Table 2 to be two folds that of the bare TiO_2 nanofibers and P25. The BJH method was employed to analyze the corresponding pore size distribution and has depicted a narrow distribution between 3-20 nm with peaking position at 4 nm (Fig. 6(b)).

Compared to bare TiO_2 nanofibers, TiO_2/SnO_2 nanofibers have demonstrated increased light absorption in the UV region and have even extended the photoresponse into the visible light region between 400-550 nm (Fig. 7(a)). A narrower bandgap of between 2.90 eV to 3.00 eV was recorded (Fig. 7(b)). Hence, it was evident that the electronic structure and optical properties of the bare TiO_2 semiconductor has been modified. As revealed by the XRD patterns, much stronger rutile TiO_2 peaks were observed in a comparison to that of rutile SnO_2. So the formation of rutile TiO_2 become a dominant factor in red-shifting the UV-vis spectrum [39]. Meanwhile, the enhanced mesoporosity and surface area of TiO_2/SnO_2 nanofibers further promote the light utilization by enabling more light scattering and reflections on the surface and within the nanostructures [40]. With this, it is suggested that the TiO_2/SnO_2 nanofibers will be able to enhance the light utilization rate for better photocatalytic activity.

The photocatalytic H_2 generation activity of the as-prepared TiO_2/SnO_2 composite nanofibers was investigated in a water/methanol sacrificial reagent system under UV-Vis light irradiation, with bare TiO_2 nanofibers and P25 used as control. Fig. 8(a) illustrates the amount of H_2 evolution as a function of UV-Vis irradiation time. Clearly, the composite nanofibers with 1% Sn and 3% Sn showed sustained stability and reactivity without sign of deactivation even after 4 hours of irradiation. There was reduction of H_2 generation rate over 6% Sn and 10% Sn nanofibers, which could be ascribed to the increased SnO_2 coverage and aggregation on the surface of TiO_2 semiconductor thus reducing the light accessibility to its active sites to initiate photocatalytic reaction [37]. Since SnO_2 by itself is not a good photocatalyst due to its large bandgap of 3.80 eV [41], overloading the TiO_2 nanofiber with SnO_2 would

subsequently retard the net composite activity [34]. Apart from this, the development of more anatase TiO_2 crystal defects due to excessive Sn may act as recombination centers for photogenerated electrons and holes [18], and consequently reduce the H_2 generation efficiency of the photocatalysts. The TiO_2/SnO_2 nanofibers with optimum ratio of 3% Sn demonstrated the highest efficiency in H_2 generation, with approximated rate of 200 μmol/hr (Fig. 8(b)). It showed an immense enhancement of 2 and 5 times H_2 generation rate in comparison to bare TiO_2 nanofibers and P25, respectively. Its evolution rate was even much higher than its nanoparticles counterpart [20, 21]. Meanwhile, the H_2 evolution rate as a function of concentration of TiO_2/SnO_2 nanofibers was investigated to obtain the optimum photocatalyst quantity for the H_2 generation. TiO_2/SnO_2 nanofibers with 3% Sn were used as it contains the optimum ratio of Sn for H_2 generation in this study. The dosage of photocatalyst is also a significant factor dominating the H_2 generation rate. As shown in Fig. 9, concentration of 0.5 g/L yielded the highest H_2 evolution rate under the same experimental conditions, below and above which the efficiency began to wane.

The efficient H_2 generation over TiO_2/SnO_2 nanofibers can be attributed to the synergistic effect from: (1) enhanced mesoporosity and surface area as verified by Fig. 6 and Table 2 thus engendering more reaction sites for reactants adsorption, mass transfer and effective light scattering (2) red-shifting of the UV-vis light absorption as well-witnessed by Fig. 7 thus improving light utilization rate; and (3) long nanofibrous structure as presented in Fig. 1 [15] as well as anatase TiO_2 - rutile TiO_2 - rutile SnO_2 ternary phases [17, 42] further inhibiting recombination of photogenerated electrons and holes. A schematic diagram (Scheme 2) was proposed based on the XRD and HRTEM results in the previous section to elucidate the probable electrons and holes transfer pathway between the ternary systems within the TiO_2/SnO_2 composite nanofibers. The transfer of photo-generated holes from the valence bands of the anatase TiO_2 and rutile SnO_2 into the valence band of the rutile TiO_2 was promoted due to the lower valence band level of the former two phases. Consequently, the photo-generated electrons on

the conduction band of the anatase TiO_2 were easily scavenged for H_2 generation since it will have longer life time. Here, methanol acted as holes scavengers and was oxidized into CO_2 and H_2O [28].

4. Conclusion

In summary, a novel-structured TiO_2/SnO_2 composite nanofibers was successfully fabricated via electrospinning an innovative precursor solution. The TiO_2/SnO_2 composite nanofibers embody excellent integration of highly enhanced physical and chemical properties for improved mass transfer, light utilization rate, and photogenerated electrons and holes separation benefiting photocatalytic H_2 generation compared to the bare TiO_2 nanofibers and the benchmark P25 photocatalysts. Thus, this TiO_2/SnO_2 composite nanofiber represents an excellent candidate for photocatalytic H_2 generation from water.

ACKNOWLEDGEMENT. The authors thank the Clean Energy Research Programme under National Research Foundation of Singapore for their research grant (Grant No. NRF2007EWT-CERP01-0420) support for this work and the support received from Public Utilities Board (PUB) of Singapore. The Scholarship provided by NTU is appreciated.

REFERENCES

[1] Zou Z, Ye J, Sayama K, Arakawa H. Direct splitting of water under visible light irradiation with an oxide semiconductor photocatalyst. Nature. 2001;414:625-7.

[2] Chen X, Shen S, Guo L, Mao SS. Semiconductor-based photocatalytic hydrogen generation. Chemical Reviews. 2010;110:6503-70.

[3] Kudo A, Miseki Y. Heterogeneous photocatalyst materials for water splitting. Chemical Society Reviews. 2009;38:253-78.

[4] Getoff N. Photoelectrochemical and photocatalytic methods of hydrogen production: A short review. International Journal of Hydrogen Energy. 1990;15:407-17.

[5] Fujishima A, Honda K. Electrochemical photolysis of water at a semiconductor electrode. Nature. 1972;238:37-8.

[6] Banerjee AN. The design, fabrication, and photocatalytic utility of nanostructured semiconductors: Focus on TiO2-based nanostructures. Nanotechnology, Science and Applications. 2011;4:35-65.

[7] Kruczynski L, Gesser HD, Turner CW, Speers EA. Porous titania glass as a photocatalyst for hydrogen production from water. Nature. 1981;291:399-401.

[8] Ashokkumar M. An overview on semiconductor particulate systems for photoproduction of hydrogen. International Journal of Hydrogen Energy. 1998;23:427-38.

[9] Nada AA, Barakat MH, Hamed HA, Mohamed NR, Veziroglu TN. Studies on the photocatalytic hydrogen production using suspended modified TiO2 photocatalysts. International Journal of Hydrogen Energy. 2005;30:687-91.

[10] Chen X, Mao SS. Titanium dioxide nanomaterials: Synthesis, properties, modifications and applications. Chemical Reviews. 2007;107:2891-959.

[11] Ni M, Leung MKH, Leung DYC, Sumathy K. A review and recent developments in photocatalytic water-splitting using TiO2 for hydrogen production. Renewable and Sustainable Energy Reviews. 2007;11:401-25.

[12] Long R, Dai Y, Huang B. Geometric and electronic properties of Sn-doped TiO2 from first-principles calculations. Journal of Physical Chemistry C. 2009;113:650-3.

[13] Uchiyama H, Imai H. Crystal growth of metastable rutile-type TixSn 1-xO2 solid solutions in an aqueous system. Chemical Communications. 2005:6014-6.

[14] Choi SK, Kim S, Lim SK, Park H. Photocatalytic comparison of TiO2 nanoparticles and electrospun TiO2 nanofibers: Effects of mesoporosity and interparticle charge transfer. Journal of Physical Chemistry C. 2010;114:16475-80.

[15] Li D, Xia Y. Electrospinning of nanofibers: Reinventing the wheel? Advanced Materials. 2004;16:1151-70.

[16] Li D, McCann JT, Xia Y, Marquez M. Electrospinning: A simple and versatile technique for producing ceramic nanofibers and nanotubes. Journal of the American Ceramic Society. 2006;89:1861-9.

[17] Liu Z, Sun DD, Guo P, Leckie JO. An efficient bicomponent TiO2/SnO2 nanofiber photocatalyst fabricated by electrospinning with a side-by-side dual spinneret method. Nano Letters. 2007;7:1081-5.

[18] Hwang SH, Kim C, Jang J. SnO2 nanoparticle embedded TiO2 nanofibers - Highly efficient photocatalyst for the degradation of rhodamine B. Catalysis Communications. 2011;12:1037-41.

[19] Chattopadhyay J, Rok Kim H, Bong Moon S, Pak D. Performance of tin doped titania hollow spheres as electrocatalysts for hydrogen and oxygen production in water electrolysis. International Journal of Hydrogen Energy. 2008;33:3270-80.

[20] Sasikala R, Shirole A, Sudarsan V, Sakuntala T, Sudakar C, Naik R, et al. Highly dispersed phase of SnO2 on TiO2 nanoparticles synthesized by polyol-mediated route: Photocatalytic activity for hydrogen generation. International Journal of Hydrogen Energy. 2009;34:3621-30.

[21] Sasikala R, Sudarsan V, Sudakar C, Naik R, Sakuntala T, Bharadwaj SR. Enhanced photocatalytic hydrogen evolution over nanometer sized Sn and Eu doped titanium oxide. International Journal of Hydrogen Energy. 2008;33:4966-73.

[22] Zhang R, Wu H, Lin D, Pan W. Preparation of necklace-structured TiO2/SnO2 hybrid nanofibers and their photocatalytic activity. Journal of the American Ceramic Society. 2009;92:2463-6.

[23] Li D, Xia Y. Fabrication of titania nanofibers by electrospinning. Nano Letters. 2003;3:555-60.

[24] Ohtani B. Preparing articles on photocatalysis - beyond the illusions, misconceptions, and speculation. Chemistry Letters. 2008;37:217-29.

[25] Liu Z, Bai H, Sun D. Facile fabrication of hierarchical porous TiO2 hollow microspheres with high photocatalytic activity for water purification. Applied Catalysis B: Environmental. 2011;104:234-8.

[26] Ng J, Xu S, Zhang X, Yang HY, Sun DD. Hybridized nanowires and cubes: A novel architecture of a heterojunctioned TiO2/SrTiO3 thin film for efficient water splitting. Advanced Functional Materials. 2010;20:4287-94.

[27] Xu S, Du AJ, Liu J, Ng J, Sun DD. Highly efficient CuO incorporated TiO2 nanotube photocatalyst for hydrogen production from water. International Journal of Hydrogen Energy. 2011;36:6538-45.

[28] Xu S, Sun DD. Significant improvement of photocatalytic hydrogen generation rate over TiO2 with deposited CuO. International Journal of Hydrogen Energy. 2009;34:6096-104.

[29] Jiang X, Herricks T, Xia Y. Monodispersed spherical colloids of titania: Synthesis, characterization, and crystallization. Advanced Materials. 2003;15:1205-9.

[30] Sigmund W, Yuh J, Park H, Maneeratana V, Pyrgiotakis G, Daga A, et al. Processing and structure relationships in electrospinning of ceramic fiber systems. Journal of the American Ceramic Society. 2006;89:395-407.

[31] Hirano M, Dozono H, Kono T. Hydrothermal synthesis and properties of solid solutions and composite nanoparticles in the TiO2-SnO2 system. Materials Research Bulletin. 2011;46:1384-90.

[32] Testino A, Bellobono IR, Buscaglia V, Canevali C, D'Arienzo M, Polizzi S, et al. Optimizing the photocatalytic properties of hydrothermal TiO2 by the control of phase composition and particle morphology. A systematic approach. Journal of the American Chemical Society. 2007;129:3564-75.

[33] Sayilkan H. Improved photocatalytic activity of Sn4+-doped and undoped TiO2 thin film coated stainless steel under UV- and VIS-irradiation. Applied Catalysis A: General. 2007;319:230-6.

[34] Lin J, Yu JC, Lo D, Lam SK. Photocatalytic activity of rutile Ti1-xSnxO2 solid solutions. Journal of Catalysis. 1999;183:368-72.

[35] Shi L, Li C, Gu H, Fang D. Morphology and properties of ultrafine SnO2-TiO2 coupled semiconductor particles. Materials Chemistry and Physics. 2000;62:62-7.

[36] Zhang Z, Shao C, Li X, Zhang L, Xue H, Wang C, et al. Electrospun nanofibers of ZnO-SnO2 heterojunction with high photocatalytic activity. Journal of Physical Chemistry C. 2010;114:7920-5.

[37] Wang C, Shao C, Zhang X, Liu Y. SnO2 nanostructures-tio2 nanofibers heterostructures: Controlled fabrication and high photocatalytic properties. Inorganic Chemistry. 2009;48:7261-8.

[38] Sing KSW. Physisorption of nitrogen by porous materials. Journal of Porous Materials. 1995;2:5-8.

[39] Mahanty S, Roy S, Sen S. Effect of Sn doping on the structural and optical properties of sol-gel TiO2 thin films. Journal of Crystal Growth. 2004;261:77-81.

[40] Liu Z, Bai H, Xu S, Sun DD. Hierarchical CuO/ZnO "corn-like" architecture for photocatalytic hydrogen generation. International Journal of Hydrogen Energy. 2011.

[41] Grätzel M. Photoelectrochemical cells. Nature. 2001;414:338-44.

[42] Liu Z, Zhang X, Nishimoto S, Jin M, Tryk DA, Murakami T, et al. Anatase TiO2 nanoparticles on rutile TiO2 nanorods: A heterogeneous nanostructure via layer-by-layer assembly. Langmuir. 2007;23:10916-9.

Captions of Tables and Figures

Table 1. Summary of physical properties of calcined TiO_2/SnO_2 composite nanofibers

Table 2. BET surface area of TiO_2/SnO_2 nanofibers with different Sn/Ti ratios

Scheme 1. Schematic diagram of the suspended system of H_2 generation reactor setup

Scheme 2. Schematic diagram of the photo-generated electrons and holes transfer between the ternary phases in the TiO_2/SnO_2 nanofibers

Figure 1. (a) FESEM images of TiO_2/SnO_2 nanofibers, (b) High magnification FESEM image of TiO_2/SnO_2 nanofibers showing detailed porous surface morphology

Figure 2. (a) TEM images and corresponding selected area electron diffraction (SAED) pattern (inset), (b) the EDS spectrum of TiO_2/SnO_2 nanofibers from the selected area, Elemental mapping of TiO_2/SnO_2 nanofibers for (c) O element, (d) Ti element, and (e) Sn element

Figure 3. (a) bright field TEM image showing TiO_2/SnO_2 nanofibers (6% Sn) with highly dispersed Sn element, (b) bright field TEM image of TiO_2/SnO_2 nanofibers, as magnified from (a) showing clear color contrast between Sn and Ti elements with Sn being darker because it is heavier, and (c) High magnification HRTEM image showing the corresponding crystal lattice of the anatase TiO_2/rutile TiO_2/rutile SnO_2 heterojunction from delineated area of (b)

Figure 4. (a) XRD patterns of electrospun TiO_2/SnO_2 nanofibers with different Sn/Ti ratios– 0% Sn (bare TiO_2), 1% Sn, 3% Sn, 6% Sn, 10% Sn and 40% Sn, all calcined at 450ºC for 30 minutes, and (b) Close-up XRD patterns of TiO_2/SnO_2 nanofibers with 0% Sn, 3% Sn, and 6% Sn between $2\theta = 22^o - 40^o$

Figure 5. (a) XPS survey spectrum for TiO_2/SnO_2 nanofibers; High resolution XPS spectrum for (b) Ti 2p, (c) Sn 3d, and (d) O 1s

Figure 6. (a) N_2 adsorption/desorption isotherm curve of TiO_2/SnO_2 nanofibers (3% Sn), and (b) BJH pore size distribution of bare TiO_2 (black) and TiO_2/SnO_2 (3% Sn) (red) nanofibers

Figure 7. (a) The UV-visible spectra of the TiO_2/SnO_2 nanofibers, and (b) the corresponding Kubelka-Munk transformed reflectance spectra to determine indirect new bandgap value for the TiO_2/SnO_2 nanofibers

Figure 8. (a) Accumulation of photocatalytic H_2 evolution over the irradiation time of 4 hours; and (b) Dependence of H_2 evolution rate on the Sn loading in photocatalysts

Figure 9. Effect of TiO_2/SnO_2 (3% Sn) nanofibers concentration on the H_2 evolution rate

Table 1 – Summary of physical properties of calcined TiO_2/SnO_2 composite nanofiber

Materials	Percentage of anatase phase[a] (%)	FHWM (degree)	Size of anatase crystal[b] (nm)
Bare TiO_2 (0% Sn)	96	0.443	18
1% Sn	83	0.558	14
3% Sn	77	0.651	12

a Calculated based on the procedure given by Ohtani, B. [24]. b Calculated by the Scherrer equation [10, 24].

Table 2 – BET surface area of TiO_2/SnO_2 nanofiber with different Sn/Ti ratios

Materials	BET surface area (m^2/g)
P25	34.4
Bare TiO_2 (0% Sn)	34.3
1% Sn	73.6
3% Sn	73.1

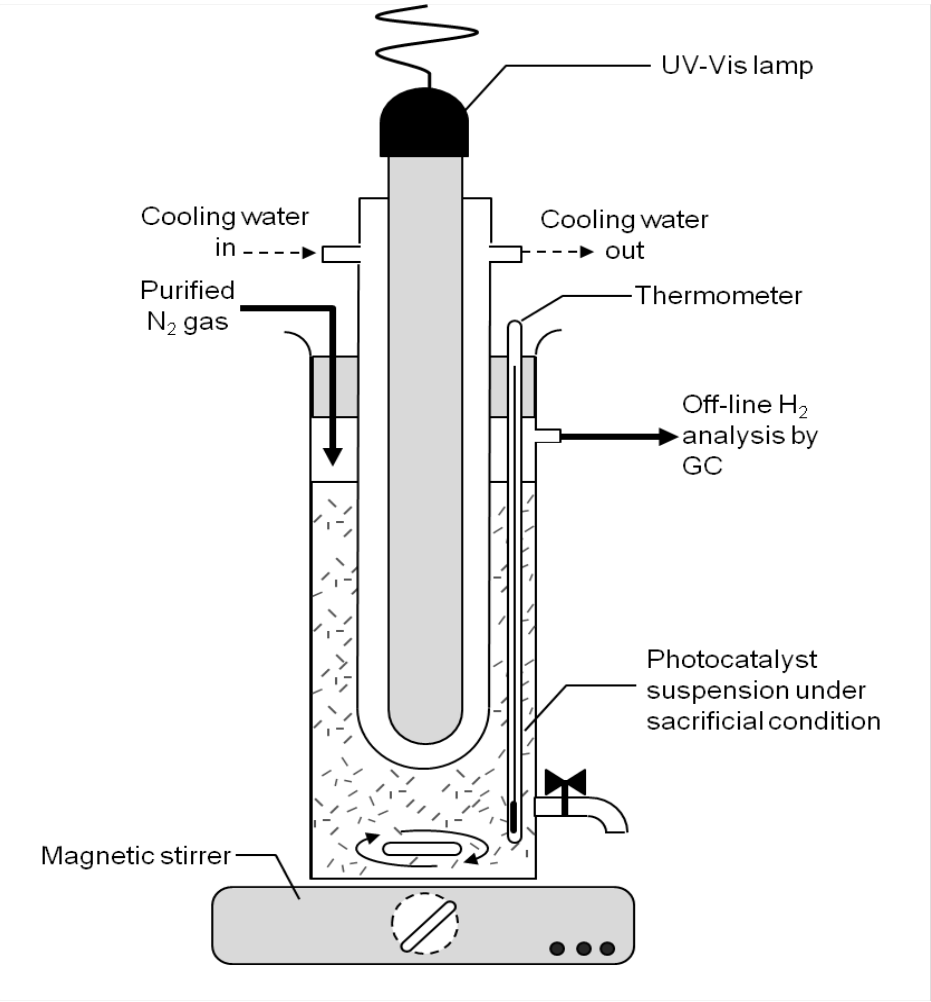
UV-Vis lamp
Cooling water in
Cooling water out
Purified N_2 gas
Thermometer
Off-line H_2 analysis by GC
Photocatalyst suspension under sacrificial condition
Magnetic stirrer

Scheme 1

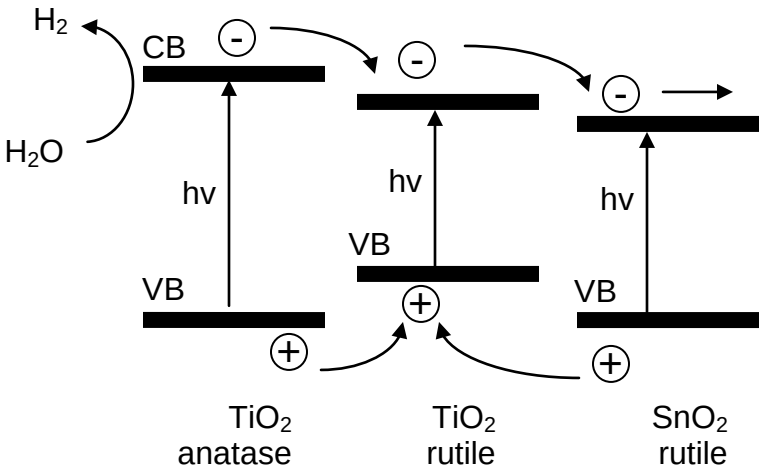
H2
H2O
CB
VB
hv
VB
hv
VB
hv
TiO2
anatase
TiO2
rutile
SnO2
rutile

Scheme 2

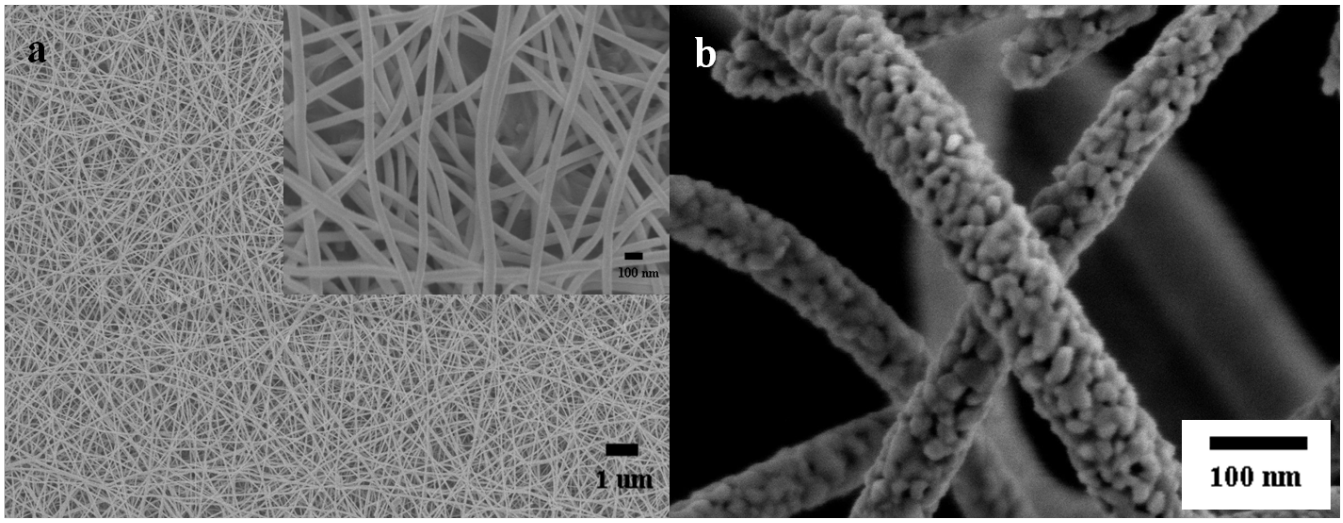

Figure 1

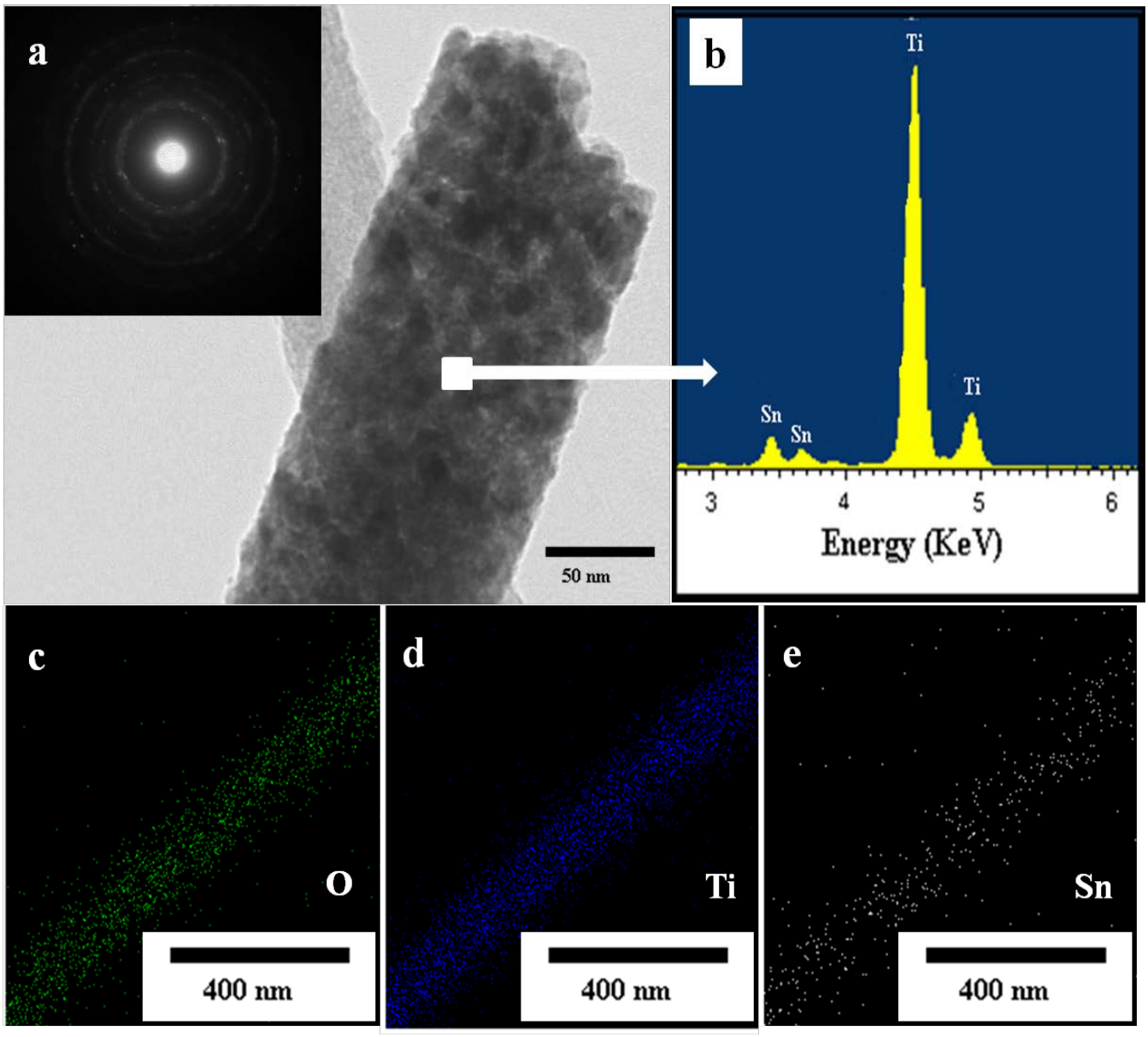
a
50 nm
b
Ti
Sn
Sn
Ti
3
4
5
6
Energy (KeV)
c
O
400 nm
d
Ti
400 nm
e
Sn
400 nm

Figure 2

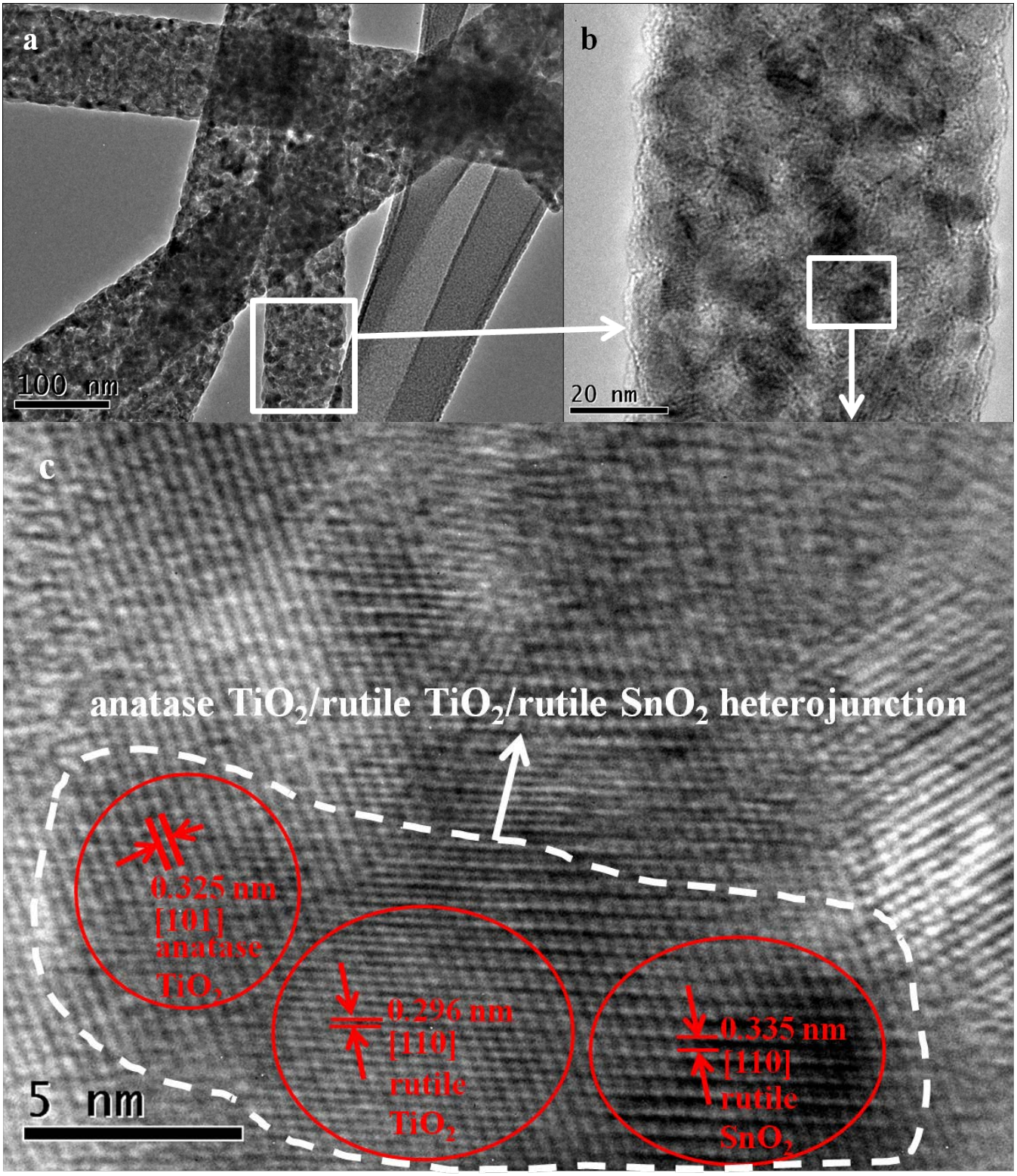
a
100 nm
b
20 nm
c
anatase TiO2/rutile TiO2/rutile SnO2 heterojunction
0.325 nm
[101]
anatase
TiO2
0.296 nm
[110]
rutile
TiO2
0.335 nm
[110]
rutile
SnO2
5 nm

Figure 3

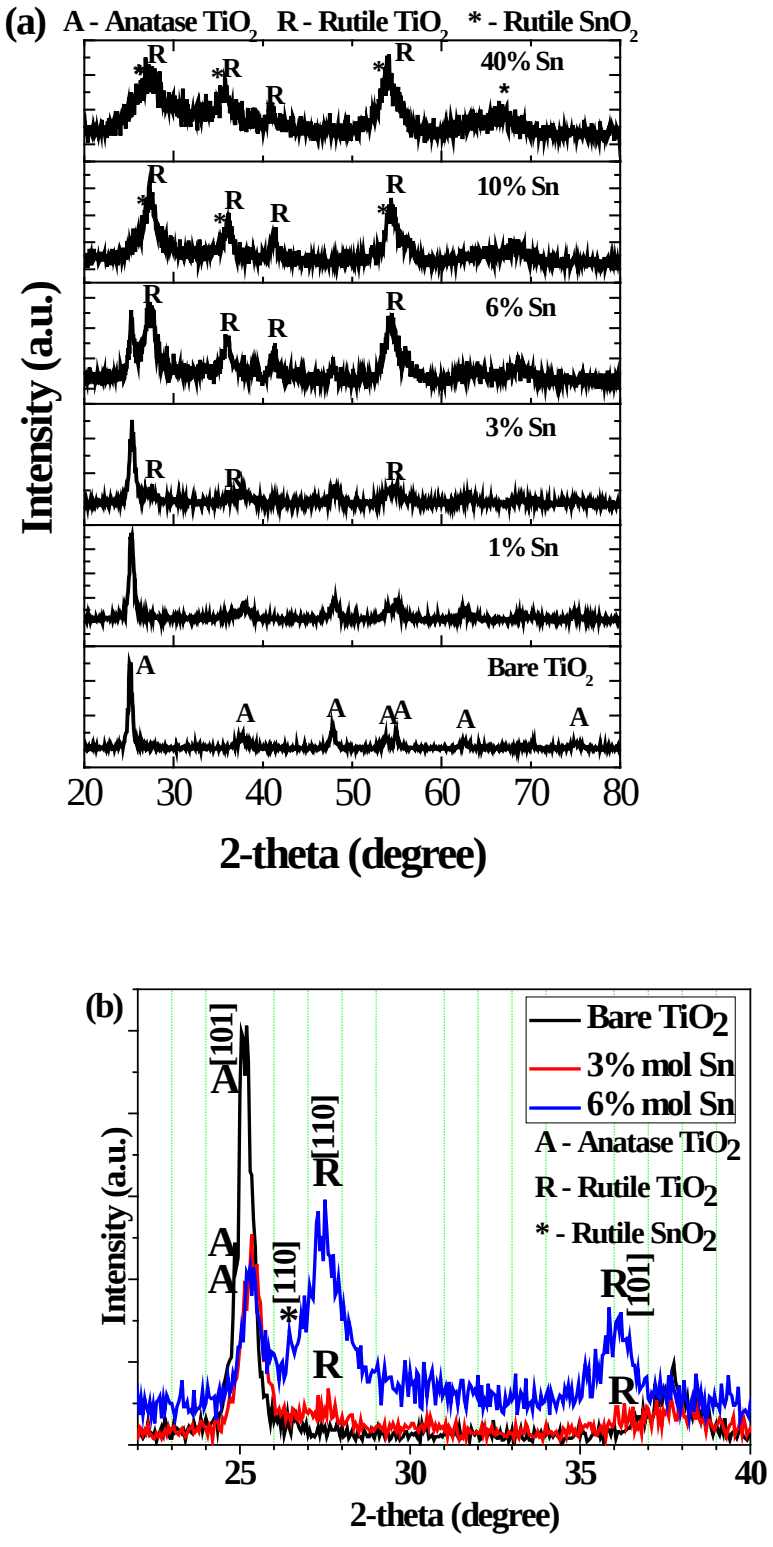
(a)
A - Anatase TiO2
R - Rutile TiO2
* - Rutile SnO2
40% Sn
10% Sn
6% Sn
3% Sn
1% Sn
Bare TiO2
Intensity (a.u.)
2-theta (degree)
(b)
Bare TiO2
3% mol Sn
6% mol Sn
A - Anatase TiO2
R - Rutile TiO2
* - Rutile SnO2
[101]
[110]
[110]
[101]
Intensity (a.u.)
2-theta (degree)

Figure 4

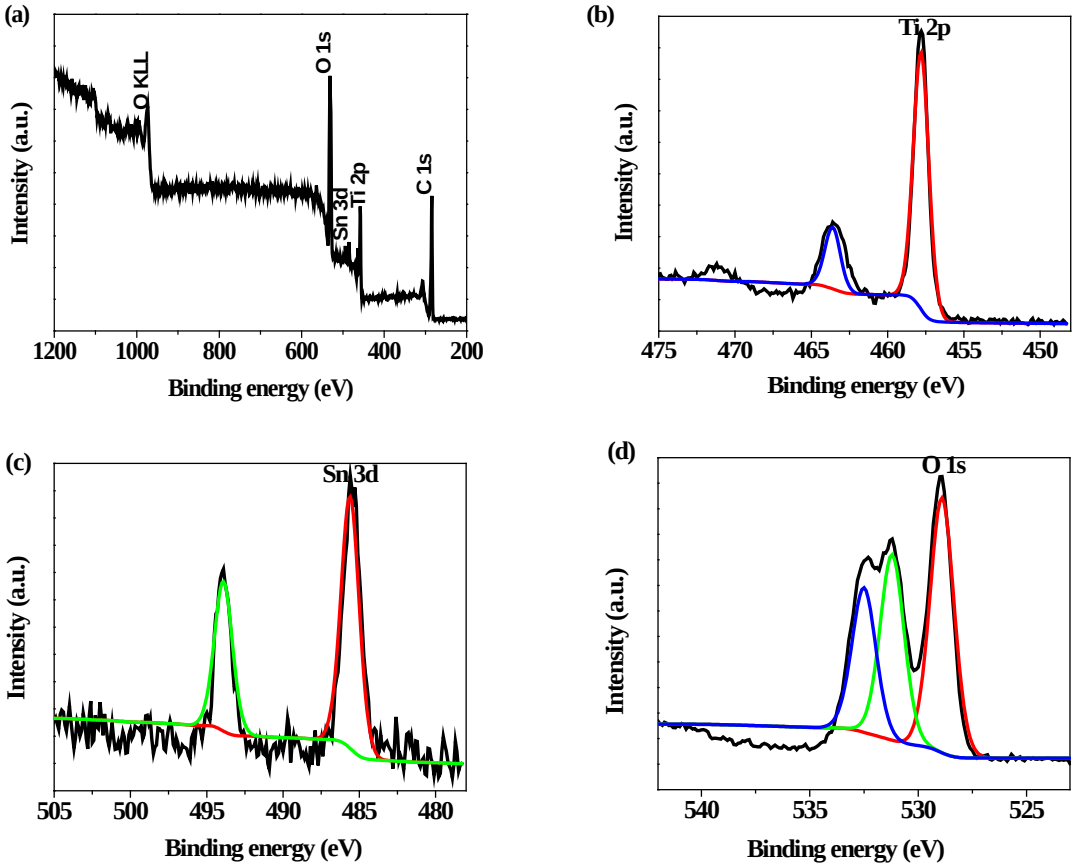
(a)
O KLL
O 1s
Sn 3d
Ti 2p
C 1s
Intensity (a.u.)
1200
1000
800
600
400
200
Binding energy (eV)
(b)
Ti 2p
Intensity (a.u.)
475
470
465
460
455
450
Binding energy (eV)
(c)
Sn 3d
Intensity (a.u.)
505
500
495
490
485
480
Binding energy (eV)
(d)
O 1s
Intensity (a.u.)
540
535
530
525
Binding energy (eV)

Figure 5

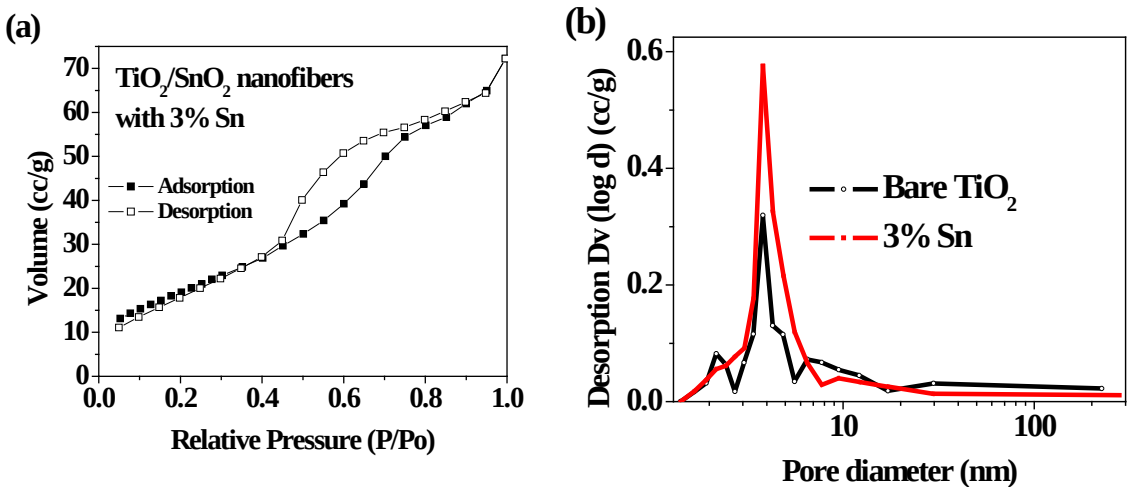
(a)
TiO2/SnO2 nanofibers
with 3% Sn
Adsorption
Desorption
Volume (cc/g)
Relative Pressure (P/Po)
0
10
20
30
40
50
60
70
0.0
0.2
0.4
0.6
0.8
1.0
(b)
Bare TiO2
3% Sn
Desorption Dv (log d) (cc/g)
Pore diameter (nm)
0.0
0.2
0.4
0.6
10
100

Figure 6

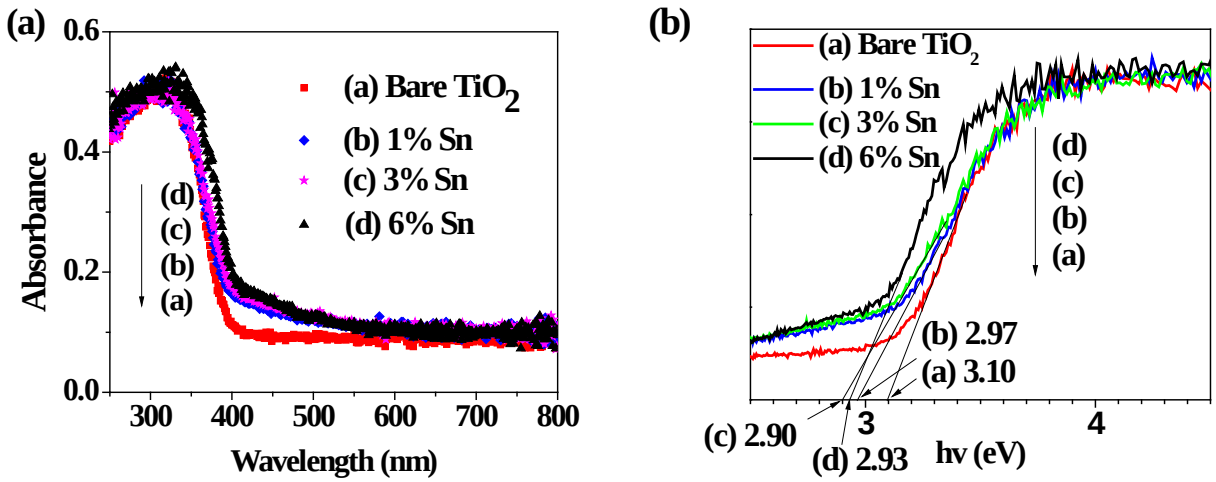
(a)
Absorbance
Wavelength (nm)
(a) Bare TiO2
(b) 1% Sn
(c) 3% Sn
(d) 6% Sn
(d)
(c)
(b)
(a)
(b)
(a) Bare TiO2
(b) 1% Sn
(c) 3% Sn
(d) 6% Sn
(d)
(c)
(b)
(a)
(b) 2.97
(a) 3.10
(c) 2.90
(d) 2.93
hv (eV)

Figure 7

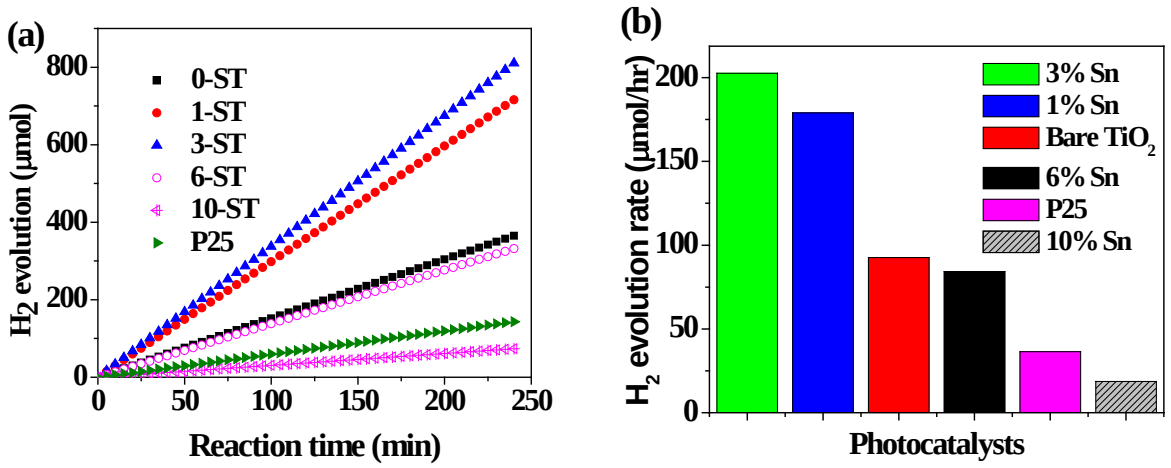
(a)
800
600
400
200
0
0
50
100
150
200
250
H2 evolution (μmol)
Reaction time (min)
0-ST
1-ST
3-ST
6-ST
10-ST
P25
(b)
200
150
100
50
0
H2 evolution rate (μmol/hr)
Photocatalysts
3% Sn
1% Sn
Bare TiO2
6% Sn
P25
10% Sn

Figure 8

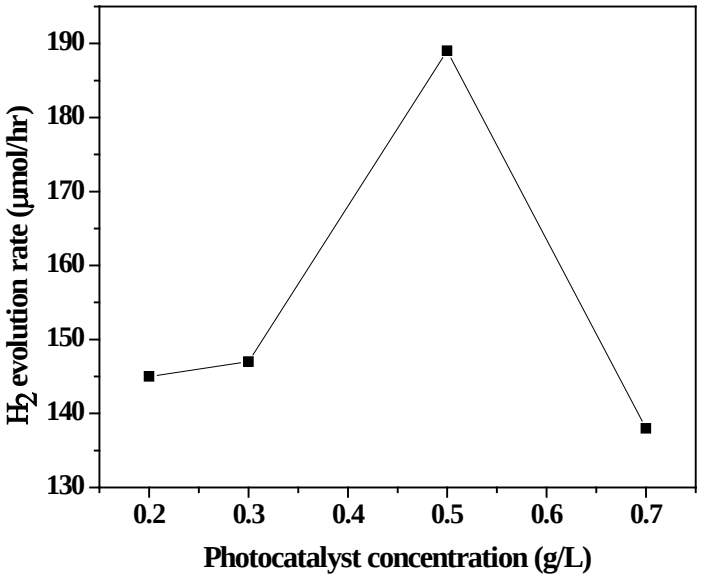
190
180
170
160
150
140
130
H2 evolution rate (μmol/hr)
0.2
0.3
0.4
0.5
0.6
0.7
Photocatalyst concentration (g/L)

Figure 9